Research Square

Preprints are preliminary reports that have not undergone peer review.
They should not be considered conclusive, used to inform clinical practice,
or referenced by the media as validated information.

Evaluation of Turbulent-Kinetic-Energy-Dissipation Relationships in the CBL Using a Combination of Doppler Lidars

Syed Abbas
syed_saqlain.abbas@uni-hohenheim.de
University of Hohenheim
Andreas Behrendt
University of Hohenheim
Verena Rajtschan
University of Hohenheim
Oliver Branch
University of Hohenheim
Linus Von Klitzing
University of Hohenheim
Volker Wulfmeyer
University of Hohenheim

Research Article

Keywords: Convective boundary layer, Doppler lidar, Turbulent kinetic energy, TKE dissipation parametrization. Vertical wind variance

Posted Date: November 18th, 2026

DOI: https://doi.org/10.21203/rs.3.rs-11667183/v1

License: This work is licensed under a Creative Commons Attribution 4.0 International License.
Read Full License

Additional Declarations: No competing interests reported.

Evaluation of Turbulent-Kinetic-Energy-Dissipation Relationships in the CBL Using a Combination of Doppler Lidars

Syed Abbas[1] • Andreas Behrendt[1] • Verena Rajtschan[2] • Oliver Branch[1]• Linus von Klitzing[1] • Volker Wulfmeyer[1]

Abstract

This study evaluates parametrizations of turbulent-kinetic-energy (TKE) dissipation (ε) in the convective boundary layer (CBL) by analyzing turbulent statistics of TKE (e), vertical wind variance ($\overline{w'^2}$), and their relationships, using high-resolution Doppler lidar data from the Land-Atmosphere Feedback Observatory (LAFO), Stuttgart, Germany. The analysis is based on 25 days with convective conditions in May to July 2021 and 2022. A combination of one vertical-pointing and one six-beam scanning Doppler lidar provided profiles of $\overline{w'^2}$, e, ε, integral time and length scales, as well as CBL depth z_i. The median profiles from 30-min averages between local morning (0900 UTC) and afternoon (1600 UTC) cover the diurnal evolution of the CBL, including its growth, peak, and decay. We found maxima of $\overline{w'^2}$, $\overline{e}$, and $\overline{\varepsilon}$ at $0.34\overline{z_i}$, $0.73\overline{z_i}$, and $0.29\overline{z_i}$, respectively, which is consistent with previous observations and large-eddy simulation studies. In addition, we also discuss distribution functions, which are very important for future stochastic parameterizations. In the lower half of the CBL, e correlates strongly with $\overline{w'^2}$ and ε with r≈0.70, while the correlation is weaker in the upper CBL with r≈0.52. The relationship between ε and $\overline{w'^2}$ follows $\overline{\varepsilon} \propto (\overline{w'^2})^{3/2}$ throughout the CBL, with r=0.83. We found a significantly higher correlation of r=0.80 when parametrizing ε with $\overline{w'^2}$ instead of parametrizing ε with e ($r = 0.46$). Machine learning models, random forest, and a multilayer perceptron independently identify $\overline{w'^2}$ as the dominant predictor, suggesting the use of a $\overline{w'^2}$-based dissipation closure in turbulence schemes for the unstable atmospheric boundary layer.

✉ Syed Abbas
syed_saqlain.abbas@uni-hohenheim.de

1 Institute of Physics and Meteorology, University of Hohenheim, Garbenstrasse 30, 70599 Stuttgart, Germany
2 Institute of Soil Sciences and Land Evaluation, University of Hohenheim, Emil-Wolff-Str. 27, 70599 Stuttgart, Germany

Keywords Convective boundary layer · Doppler lidar· Turbulent kinetic energy · TKE dissipation parametrization. Vertical wind variance

1 Introduction

Turbulent transport in the convective boundary layer (CBL) governs the exchange of heat, moisture, momentum, and trace constituents between the land surface and the atmosphere (e.g. Stull 1988; Nieuwstadt and Duynkerke 1996; Holtslag et al. 2013; Li et al. 2017). Accurate representation of these processes is essential for weather prediction and climate projections as well as for air quality forecasting and renewable energy assessment. Despite its importance, turbulence parametrization in numerical weather prediction (NWP) and climate models still exhibit large uncertainties, degrading simulations of wind, temperature, and moisture (e.g.Wyngaard 2004; Honnert et al. 2011; Holtslag et al. 2013; Hu et al. 2013; Bodini et al. 2018; Wulfmeyer et al. 2024) and the modelling of resulting processes such as convection initiation (e.g. Wilson and Roberts 2006; Trier et al. 2004). This problem is related to the fact that current turbulence parametrization schemes in NWP models are inadequate to capture the complexity and variability of boundary layer turbulence dynamics, leading to significant uncertainties in the model results (e.g. Berg and Zhong 2005; Steeneveld et al. 2008; Storm et al. 2009; Banta et al. 2013).

In the CBL, turbulent eddies span a wide range of spatial and temporal scales (e.g., Lenschow and Stankov 1986; Stull 1988). The largest eddies scale with the CBL depth, draw energy from the surface and transfer it through a cascade of progressively smaller scales until viscous effects dissipate this turbulent kinetic energy (TKE, e) into heat at the Kolmogorov microscale (e.g. Stull 1988; Kaimal and Finnigan 1994; O'Connor et al. 2010). Key quantities in higher-order turbulence parameterizations are vertical wind variance $\overline{w'^2}$, e, TKE dissipation ε, and molecular destruction (e.g. Yang et al. 2017; Zhou et al. 2020; Wulfmeyer et al. 2024). Their accurate representation in atmospheric models is crucial for simulating vertical mixing of heat, moisture, and momentum. Vertically resolved observations of $\overline{w'^2}$, e, and ε as well as the relationships between them are essential for evaluating the representation of turbulent processes in boundary-layer parameterizations.

Previous field studies have shown distinct vertical and temporal patterns in $\overline{w'^2}$, e, and ε within the CBL. Using turbulence measurements from sonic anemometers on towers, tethered balloons, and airborne platforms, Darbieu et al. (2015) demonstrated that the vertical and horizontal components of TKE evolve differently during the afternoon transition, with $\overline{w'^2}$ decreasing earlier in the upper boundary layer than the horizontal components. Similarly, Lampert et al. (2016) observed changes in turbulence anisotropy, with $\overline{w'^2}$ decreasing faster than the horizontal components of TKE in the upper part of the CBL. A similar behavior is found from long-term Land-Atmosphere Feedback Observatory (LAFO) Doppler lidars (DLs) observations (Abbas et al. 2026, manuscript submitted to J. Appl. Meteorol. Climatol.), motivating the present investigation of how these differences are reflected in TKE dissipation and its parametrization. Wulfmeyer et al. (2024) found a strong nonlinear relationship between TKE dissipation and $\overline{w'^2}$ for the entire CBL, indicating that TKE dissipation can be directly estimated from $\overline{w'^2}$. Several other studies have used DLs to investigate vertical structure and temporal variability of $\overline{w'^2}$, TKE, and TKE dissipation. Vertical pointing DLs have been used for derivation of $\overline{w'^2}$ and higher-order moments (e.g., Bonin et al. 2016; Berg et al. 2017; Dewani et al. 2023; Wulfmeyer et al. 2024). The scanning DLs in the six-beam scanning mode were used to derive three-velocity variance, Reynold stresses, and TKE (Sathe et al. 2015; Bonin et al. 2017). However, none of these studies provide simultaneous high-resolution measurements of $\overline{w'^2}$, TKE, and TKE dissipation.

Turbulence intensity and CBL structure vary strongly from day to day because of changes in soil moisture, surface fluxes and their partitioning, surface heterogeneity, entrainment, and large-scale forcing. This sensitivity highlights the need for long-term observational datasets from the surface to the lower troposphere that span a range of surface-flux regimes and meteorological conditions. An important step in this direction was the Land–Atmosphere Feedback Experiment (LAFE; Wulfmeyer et al. 2018) at the ARM Southern Great Plains site demonstrating how a synergy of scanning lidars and complementary measurements can be used to evaluate turbulence parametrization in large-eddy simulation (LES) and NWP models (e.g. Wulfmeyer et al. 2016; Wulfmeyer et al. 2018). LAFE provided the foundation of a comprehensive land-atmosphere (L-A) study using

observations from the LAFO at the University of Hohenheim in Stuttgart, Germany (Späth et al. 2023), as well as the establishment of the GEWEX LAFO (GLAFO) project[1] (Wulfmeyer et al. 2020). At LAFO, a large suite of instruments is deployed for the simultaneous observation of processes in the soil, the land cover, and the lower troposphere as well as exchange processes between the different compartments.

In this study, we focus on two DLs that operate continuously with high spatio-temporal resolutions at LAFO. Typically, as also for this study, one DL is running in continuous vertical-staring mode providing time series of vertical wind velocity. The second DL is operated in a six-beam scanning mode (Bonin et al. 2017). Using data from these two lidars, we derive atmospheric variables, such as horizontal wind speed V_h and shear, as well as turbulent quantities in the CBL, including $\overline{w'^2}$, e, ε, integral time scale $\tau_{w'}$, and the integral length scales $R_{w'}$. These variables and their relationships are crucial for characterizing CBL turbulence and testing turbulence parametrizations (Bonin et al. 2017).

The main objective of this study is to present a statistical analysis of $\overline{w'^2}$, TKE, and ε profiles in the CBL, as well as their relationships, and to evaluate the existing TKE-based dissipation scaling. In this study, we focus on meteorological conditions characterized by clear sky conditions or low cloud coverage. Two machine learning (ML) approaches, namely multilayer perceptron (MLP) and random forest (RF), are trained to estimate TKE dissipation using turbulence-related and surface variables and to identify the most influential predictors.

Following this introduction, Section 2 reviews current higher-order turbulence parameterizations, particularly the MYNN scheme as a case study to examine how the TKE dissipation term is represented in the TKE budget equation. Section 3 describes the experimental site, the Doppler lidar systems, prevailing meteorological conditions, criteria for day selection, and the methodology for deriving turbulent quantities in the CBL. Our results are presented in Section 4, followed by a discussion in Section 5. Finally, Section 6 concludes the study with a summary of key findings and an outlook for future work.

2 Turbulence Parameterizations

[1] See also https://www.gewex.org/project/glafo

The turbulent transport of heat, moisture, and momentum in the CBL, including entrainment at the CBL top is represented by PBL schemes in NWP models. The Weather Research & Forecasting Model (WRF) includes several widely used TKE-based schemes such as MYJ (Janjić 1994), MYNN (Nakanishi and Niino 2006), and BouLac (Bougeault and Lacarrère 1989). A full description of these schemes, together with the associated references, is provided in the WRF User Guide (NCAR 2026).

In these TKE-based schemes, the MYNN scheme has become widely used in boundary layer turbulence studies. In MYNN, $\overline{w'^2}$, TKE and ε are essential components for representing CBL turbulence (Nakanishi-Niino 2009; Olson et al. 2019). Under horizontally homogeneous conditions, the budget of *e* is given by (e.g., Stull, 1988; Nilsson et al. 2016a):

$$\frac{\partial e}{\partial t} = -\frac{\partial}{\partial z}\left[\overline{w'\left(e + \frac{p'}{\rho_0}\right)}\right] - \overline{u'w'}\frac{\partial \bar{u}}{\partial z} - \overline{v'w'}\frac{\partial \bar{v}}{\partial z} + \frac{g}{\theta_0}\overline{w'\theta'} - \varepsilon, \quad (1)$$

where e represents TKE, t is time, and u', v', w' are the fluctuations of the wind components u, v, and w in the longitudinal, latitudinal, and vertical directions, respectively. p' is the fluctuation of atmospheric pressure p, ρ_0 is air density, $\overline{u'w'}$ and $\overline{v'w'}$ are the momentum fluxes, g is the acceleration due to gravity, θ_0 is potential temperature, and $\overline{w'\theta'}$ is the buoyancy flux. In this version of Eq. 1, horizontal homogeneous conditions are assumed so that the advection term and the horizontal gradients of fluxes are neglected. In the CBL, TKE dissipation ε influences the evolution of TKE. TKE and the characteristic dissipation length scales are the primary quantities used in conventional TKE dissipation parametrizations (Nakanishi and Niino 2009; Zhou et al. 2020; Lv et al. 2023). TKE dissipation is usually parametrized through a TKE-based scaling relationship based on the characteristic size and strength of turbulent eddies with

$$\varepsilon \propto \frac{e^{3/2}}{C_e L_T}, \quad (2)$$

where L_T is the turbulence dissipation length scale in the CBL and C_e a closure coefficient (Nakanishi-Niino 2009).

In most diagnostic models following Mellor and Yamada (1974), L_T is parameterized with

$$L_T = c\frac{\int_0^{zi} e\, z\, dz}{\int_0^{zi} e\, dz}, \quad (3)$$

where c = 0.23 is an empirical constant, z is height above sea level, and z_i is the CBL depth. Some recent studies have highlighted limitations of this relation. For example, Bodini et al. (2020) showed that the MYNN dissipation scheme, a key parameter in turbulence parametrization, shows strong biases near the surface, particularly under stable conditions. Zhou et al. (2019, 2020) and Lv et al. (2023) discussed the fact that e not only contains motions that contribute to the inertial-subrange cascade, but also horizontal wind variance associated with non-isotropic large-scale structures such as roll, cellular convection, and mesoscale circulations. These large-scale features distort energy partitioning and weaken the relationship between e and ε. In contrast, $\overline{w'^2}$ directly reflects the vertical motions that transport energy into the inertial subrange. Therefore, it provides a stronger physical basis for describing the energy transfer towards dissipation scales and is suggested as a more meaningful predictor of ε than bulk TKE in the CBL. Motivated by this, Wulfmeyer et al. (2024) proposed a dissipation scaling of the form

$$\varepsilon \propto (\overline{w'^2})^{\frac{3}{2}}, \tag{4}$$

offering a physically consistent TKE dissipation scaling in the CBL. This scaling will be investigated further in this work.

3 Observational Site, Instrumentation, and Observation Period

3.1 The Land-Atmosphere Feedback Observatory (LAFO)

The LAFO site is located at the University of Hohenheim in southwestern Germany (48.714° N, 9.184° E), approximately 7 km south of the city center of Stuttgart, and 3 km north of Stuttgart Airport (Späth et al. 2023). This site was established in May 2018 in the vicinity of the university's agriculture research farm at Heidfeldhof. This facility is surrounded by a forest to the west-southwest, and consists of 26 different agricultural fields, mostly with maize, rapeseed, wheat, triticale, barley, and other crops within an area of 84 ha (Späth et al. 2023, Fig. 1). The terrain at the LAFO site is relatively flat, with an elevation range between 390 and 420 m above mean sea level. Typical mean temperature ranges are from about 0 °C in winter to around 18 °C in summer. The main purpose of this observatory is to study L-A interactions and feedback processes using a unique combination of in-situ and remote sensing instruments providing simultaneous

measurements of key variables in the L-A system from the soil to the land cover – in this case crops – and the lower troposphere.

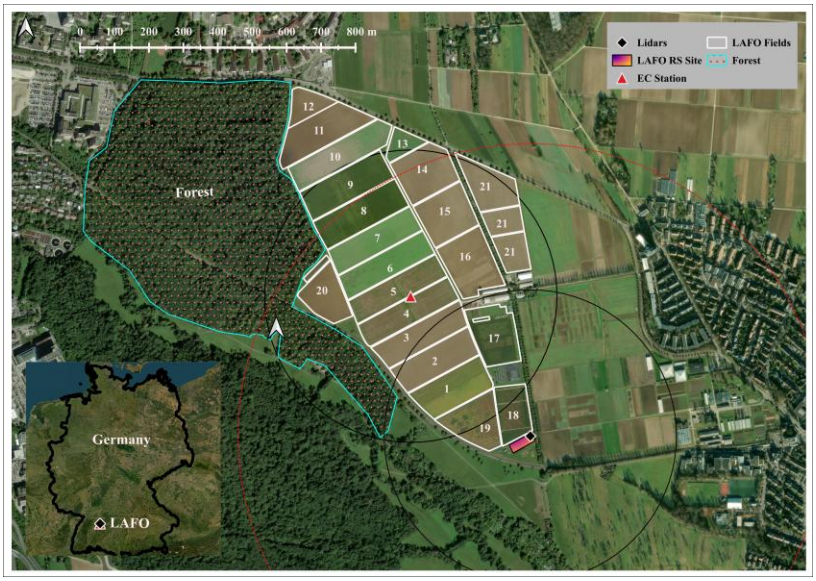


Fig. 1 Overview of the LAFO site, highlighting the installation of the vertically pointing and six-beam scanning DLs at the LAFO remote sensing (RS) site. The eddy covariance station is located approximately 650 m northwest of the RS site. Two circles with a 500 m (black line) and 1000 m (red dotted line) radiuses are drawn around Doppler lidar's location. EC station is located between fields 4 and 5. The map was created using QGIS with the Google Imagery Hybrid basemap (2025)

3.2 Surface Measurements and Meteorological Conditions

In this work, we focus on meteorological conditions with no or only low cloud cover (cloud fraction < 35%) between 0600-1800 UTC and no precipitation. We selected 25 typical days from May to July in 2021 and 2022, characterized by strong convective conditions at the LAFO. In 2021, the selected dates are 8, 9, and 31 May; 1, 2, 16, and 17 June; and 2, 10, and 18 July. In 2022, the selected dates are 14 May; 10, 14, and 25 June; and 2, 3, 8, 12, 14, 16, 17, 18, 19, 22, and 24 July. Surface wind speeds are generally below 5 m s^{-1} on these days, with a prevailing south-easterly flow.

Figure 2a and 2b show the 30-min mean net radiation $\langle\overline{Q_n}\rangle$ and 2 m air temperature $\langle\overline{T_{2m}}\rangle$, respectively, averaged over all selected days measured at a station located approximately 600 m northwest of the LAFO remote sensing site. $\langle\overline{Q_n}\rangle$ followed a typical diurnal cycle: It changed from negative to positive values at around 0600 UTC with the onset of incoming solar radiation and continued to rise through the morning. At local noon (1130 UTC), $\langle\overline{Q_n}\rangle$ reached 630±10 W m^{-2} and peaked 1 h later at 1230 UTC with a maximum value of

650 ± 15 W m^{-2}. In the afternoon, it gradually decreased until the evening, becoming negative again after about 2000 UTC. The variability in $\langle \overline{Q_n} \rangle$ was generally smaller in the morning and slightly larger in the afternoon. Figure 2b shows that $\langle \overline{T_{2m}} \rangle$ exhibited a minimum of 11.2 ± 4.3 °C at about 0500 UTC, just before sunrise, and a maximum of 25.6 ± 4.0 °C at 1630 UTC. As expected, the temperature lagged the net radiation (Renner et al. 2019; Wu et al. 2023). Figure 2c shows the distribution of 30-min wind speed and wind direction during the daytime period of 0600 to 1800 UTC for the selected days. The prevailing 2-m mean wind direction $\overline{\theta_s}$ was from the southeast (120°-160°) with a typical wind speed $\overline{V_s}$ of up to 3 m s^{-1}.

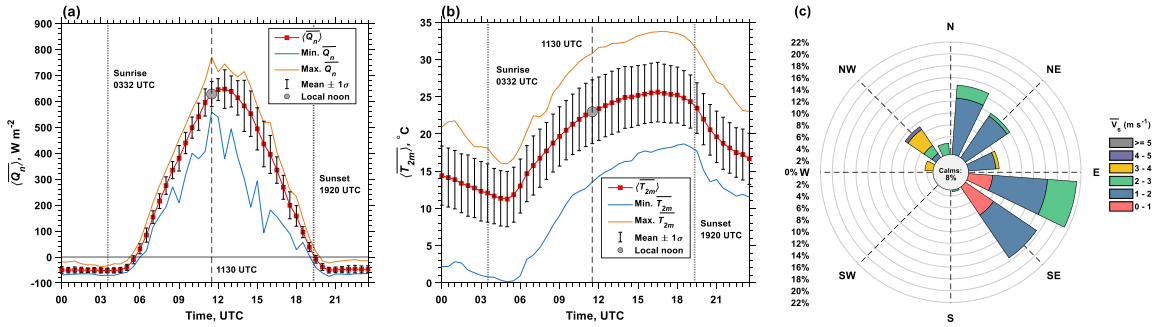


Fig. 2 30-min averages over 25 convective days from May to July 2021 and 2022: (a) net radiation, $\langle \overline{Q_n} \rangle$, (b) temperature at 2 m height, $\langle \overline{T_{2m}} \rangle$, (c) wind rose showing the frequency distribution of horizontal wind speed, $\langle \overline{V_s} \rangle$; and horizontal wind direction, $\langle \overline{\theta_s} \rangle$. Local noon (1130 UTC) is marked with circles. Error bars indicate 1-sigma standard deviations, and maximum/minimum values are also shown. The black dotted vertical lines in (a) and (b) show the mean time of sunrise and sunset

3.3 Operation Modes and Analysis Methods

3.3.1 Doppler Lidars Systems

We used two DL systems Streamline XR of Halo Photonics to measure radial wind velocities up to a maximum range of 10 km. These lidars emit laser pulses at a wavelength of 1.5 µm with a pulse repetition frequency of 10 kHz. Aerosol particles in the atmosphere scatter these laser pulses. The backscattered signals, shifted in frequency by the Doppler effect, are received by coherent detection and used to determine the line-of-sight (LOS) wind velocity.

One DL operated in continuous vertical-staring mode and the second in a six-beam scanning mode, both with a temporal resolution of 1 s and a range resolution of 30 m. Previous studies demonstrated that these spatial and temporal resolutions are sufficient to resolve turbulent velocity fluctuations down to the inertial subrange (Lenschow et al. 2000;

Wulfmeyer et al. 2016; Wulfmeyer et al. 2024). Both systems provide LOS wind velocity, signal-to-noise ratio (SNR), and attenuated backscatter β.

3.3.1 Profiling of Turbulent Variables

We determined the profiles of vertical wind variance $\overline{w'^2}$ and TKE dissipation ε by separating instrumental noise from the atmospheric turbulence in the inertial subrange and by applying Taylor's hypothesis to the atmospheric turbulent fluctuations as presented in Lenschow et al. (2000). The processing steps are explained in detail by Wulfmeyer et al. (2016, 2024). In the inertial subrange, turbulence is assumed to become spatially isotropic so that, for small lags, the autocovariance function (ACF) of the time series of the vertical wind fluctuations $w'(z,t)$ can be approximated at each height z via the structure function in the time domain (Monin and Yaglom 1979; Wulfmeyer et al. 2016; Bonin et al. 2016; Wulfmeyer et al. 2024) according to

$$A_{w'}(\tau) = \overline{w'^2} - k_{w'}\tau^{2/3} = \overline{w'^2} - \lfloor \varepsilon V_h \rfloor^{2/3}\tau^{2/3}. \quad (5)$$

Here, $A_{w'}(\tau)$ is the ACF at time lag τ, $k_{w'} = \lfloor \varepsilon V_h \rfloor^{2/3}$ is the structure function coefficient, $\boldsymbol{\varepsilon}$ is the TKE dissipation, and V_h is the horizontal wind speed. The profiles of $\overline{w'^2}$ and $\overline{\varepsilon^2}$ are derived simultaneously by fitting Eq. 5 to the observed ACF at each height.

The integral time scale $\tau_{w'}$ characterizes the mean time of the eddies in the inertial subrange advecting past the observing point (see Eq. 42 in Wulfmeyer et al. 2016). It is determined with

$$\tau_{w'} = \frac{5}{2}\left[\frac{\overline{w'^2}}{k_{w'}}\right]^{3/2}. \quad (6)$$

Once $\tau_{w'}$ is known, the corresponding integral length scale is obtained with

$$R_w = \tau_{w'} V_h \,. \quad (7)$$

To assess whether $w'(z,t)$ follows inertial subrange turbulence, we analyzed $A_{w'}(\tau, z)$ using vertical-pointing DL data with 1 s and 30 m resolution. Following Wulfmeyer et al. (2024), the inertial subrange for 1-s data is best represented by lag times between 7 and 25 s so that the inertial subrange is separated. Using this lag range, a structure function fit provides robust estimates of $\overline{w'^2}$ and $k_{w'}$. Once $k_{w'}$ is determined, the TKE dissipation ε_{obs} observed with the DL is obtained with

$$\varepsilon_{obs} = \frac{\left[k_{w'}\right]^{3/2}}{V_h}. \quad (8)$$

The required radial velocity profiles are obtained from the six-beam scanning DL scanning configuration, consisting of five inclined beams at an elevation angle of 45° at five azimuth angles of 0°, 72°, 144°, 216°, and 288° including sixth beam pointing vertically. The profiles of V_h are retrieved from these six-beam DL measurements with a temporal resolution of 90 s and a spatial resolution of 21 m (Newsom et al. 2017). As described by Bonin et al. (2017), the Reynolds stress tensor **R** is computed from the radial velocity variances using six-beam data, which is fundamental for characterizing turbulent statistics. This method requires at least six radial velocity variances to obtain the six independent components of **R**. The tensor contains second-order turbulence moments: its diagonal elements represent the velocity variances $\overline{u'^2}$, $\overline{v'^2}$, and $\overline{w'^2}$ represent the streamwise, cross-stream, and vertical velocity variances, respectively, while $\overline{u'v'}$, $\overline{u'w'}$, and $\overline{v'w'}$represent the corresponding turbulence covariances of the turbulent wind field. All the components of **R** are computed from the six-beam DL data with

$$\mathbf{R} = \begin{bmatrix} \overline{u'^2} & \overline{u'v'} & \overline{u'w'} \\ \overline{v'u'} & \overline{v'^2} & \overline{v'w'} \\ \overline{w'u'} & \overline{w'v'} & \overline{w'^2} \end{bmatrix}. \quad (9)$$

e is then obtained from the diagonal elements of R with

$$e = \frac{1}{2}\left(\overline{u'^2} + \overline{v'^2} + \overline{w'^2}\right). \quad (10)$$

3.4 Power Spectra of the Turbulent Flow

The power spectra of vertical wind velocity at different heights show the characteristic structure of turbulence in the CBL. Figure 3 shows the power spectral density (PSD) of $w'(z,t)$ of two typical days (31 May 2021 and 1 June 2021) between 1300 and 1400 UTC as examples, showing the characteristics of a fully developed CBL. For both days, at low frequencies (~0.0008-0.001 Hz), the turbulence spectrum is dominated by large-scale energy-containing eddies, with nearly height-independent peaks at 275 m, 675 m, and 1075 m. For these heights, at intermediate frequency range (~0.0032 to 0.075 Hz), the spectral power decreases approximately following the theoretical Kolmogorov -5/3 slope, showing the inertial subrange. This behavior is consistent with locally isotropic turbulence and

supports Taylor's frozen turbulence hypothesis. At high frequencies, the spectra decrease rapidly, showing the transition towards the dissipation range.

Strong surface heating on both days and all selected study days led to a well-developed CBL, ensuring that the power spectra were suitable for studying turbulence motions in the inertial subrange. This region is particularly important for deriving $k_{w'}$ and, subsequently, the TKE dissipation.

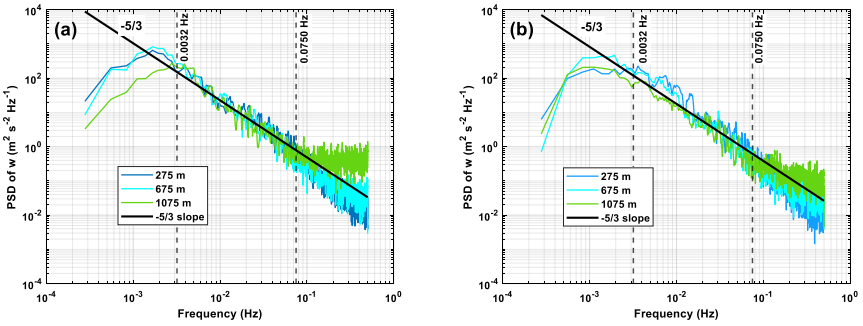


Fig. 3 Power spectral densities of vertical wind fluctuations on double-logarithm scales at different heights shown with coloured lines between 1300 to 1400 UTC on (a) 31 May 2021, and (b) 1 June 2021, at LAFO. The solid black line shows the theoretical fit of -5/3 Kolmogorov slope to the energy spectrum, while the vertical dashed lines show the intermediate frequency range used to identify the inertial subrange

3.5 Convective Boundary Layer Depth and Cloud Base Height

In our analysis, determining the 30-min mean CBL depth $\overline{z_i}$ during daytime is an important step. We estimate $\overline{z_i}$ from profiles of $\overline{w'^2}$ derived from vertical-pointing DL (Tucker et al. 2009). However, as noted by Bonin et al. (2018), these variance profiles can be misleading in the presence of internal gravity waves at the CBL top, leading to an overestimation of $\overline{z_i}$. In such conditions, high-frequency filtering of vertical wind data is necessary to isolate the true turbulent signal. To determine $\overline{z_i}$, Bonin et al. (2018) developed a fuzzy logic algorithm that integrates multiple variance metrics from various lidar scan types: velocity-azimuth display, range height indicator, vertical stare, and horizontal shallow stare. For our specific objective in daytime, $\overline{z_i}$ was determined using a two-step fuzzy-logic approach, following the general concepts of Bonin et al. (2018) and Smith and Carline (2024). In the first step, $\overline{z_i}$ was estimated from the active turbulence mixing using vertical velocity variance and high-frequency variance. The high-frequency variance helps to reduce the influence of non-turbulent low-frequency motions such as gravity waves. Instead of applying the fixed vertical-wind variance threshold of 0.02-0.08 m^2s^{-2} used by Bonin et al. (2018), we applied a time-dependent threshold over a two-hour moving window during the

297 daytime period (0500-2100 UTC) to improve the determination of $\overline{z_i}$. In a second step, the
298 first estimation was refined using β and SNR gradients near the same height, since the
299 transition from mixed layer to free troposphere is often marked by a strong gradient in
300 aerosol backscatter. The final CBL height was defined as the top of the surface-connected
301 mixed layer where the combined fuzzy membership exceeds 0.5.
302 Figure 4a shows the 30-min-average CBL depth $\overline{z_i}$ for each of the 25 days of our study.
303 The corresponding mean diurnal evolution, obtained by averaging all days in 30-min
304 intervals, is shown in Fig. 4b. The mean CBL depth $\langle\overline{z_i}\rangle$, averaged over all selected days,
305 reaches a maximum of 1.51 ± 0.7 km at 1515 UTC. Interestingly, this peak occurs 3.75
306 hours after local noon. The growth phase of the CBL is slower than its subsequent decay,
307 resulting in a pronounced asymmetry in the daytime diurnal cycle of $\overline{z_i}$.
308 Cloud-base height (CBH) was derived from the attenuated backscatter profiles of the
309 vertically pointing Doppler lidar at a temporal resolution of 1 s. A cloud layer was
310 identified when β exceeded $2 \times 10^{-5}\ \mathrm{m^{-1}\ sr^{-1}}$. The layer was confirmed only if the
311 backscatter decreased by at least a factor of 10 within approximately 250 m above the peak,
312 indicating a thick, optically dense cloud. To locate the cloud base, the algorithm searched
313 downward from the top of the candidate layer and identified the first height where the
314 vertical β gradient exceeded 25% of the maximum gradient within that range. Newsom et
315 al. (2019b) describes a similar cloud-base detection algorithm based on a threshold in β,
316 strong signal attenuation above the cloud top, and a gradient-based criterion for identifying
317 the cloud base in Doppler lidar data.
318 As shown in Figure 4c and 4d, cloud occurrence was low across almost all selected days
319 between 0600-1800 UTC: Clouds were detected in only 4.40% of the profiles (45,572 of
320 1,036,840 valid 1 s DL profiles). Clouds were not detected on nine days, and cloud
321 occurrence remained below 1% for 15 days. The highest cloud occurrence was observed
322 on 2 July 2021 (34.73%), followed by 8 August 2022 (20.65%), 24 August 2022 (12.86%),
323 and 10 July 2021 (12.23%). This confirms that the selected days were mostly cloud-free in
324 the lower 3 km.

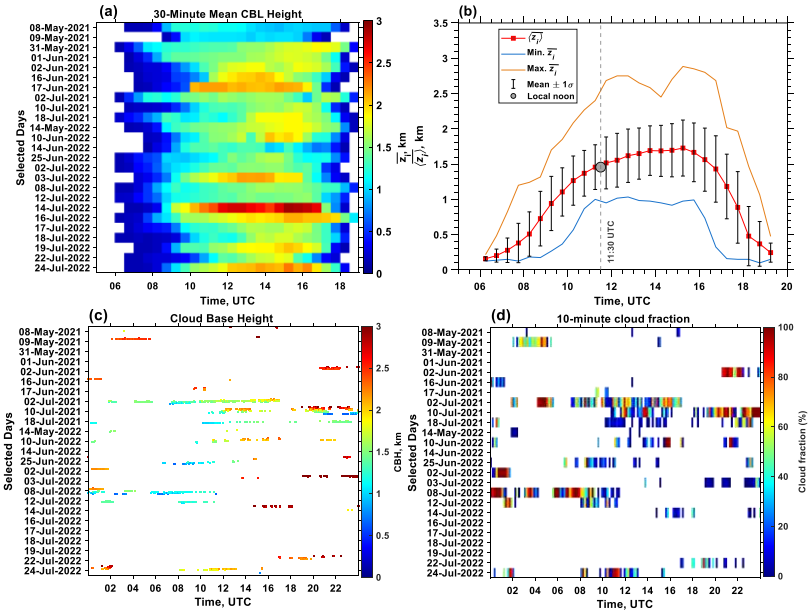


Fig. 4 (a) 30-min average CBL depth $\overline{z_i}$ for all selected days between 0500 and 1900 UTC. (b) Mean diurnal evolution of the CBL depth $\langle \overline{z_i} \rangle$ averaged over all selected 25 days in 30-min intervals as well as minimum and maximum values. Error bars indicate ± 1 standard deviation. Local noon at 1130 UTC is marked with a grey filled circle. (c) Cloud base height derived from 1-s DL profiles and (d) cloud fraction averaged over 10-min time windows during the daily analysis period of 0600 to1800 UTC for all selected days

3.7 Daily Evolution of Turbulence in the CBL

Figure 5 shows the diurnal cycles for the two representative clear-sky days 31 May 2021 and 1 June 2021 at LAFO. The vertical pointing DL provides $w'_{tot}(z,t)$ with resolutions of 30 m and 1 s. From these time series, $\overline{w'^2}$, e, the observed TKE dissipation $\overline{\varepsilon_{obs}}$, $\overline{\tau_{w'}}$, and skewness $\overline{S_{w'}}$ are derived using resolutions of 50 m and 10 minutes.

The time-height plot of $w'_{tot}(z,t)$ in Fig. 5a shows the difference in turbulence intensity between nighttime and daytime. At night, the turbulence is weak due to thermally stable stratification, while daytime is characterized by intense turbulent mixing in the CBL. Each day after sunrise shows the typical convective evolution: rapid morning growth of the CBL, intensifies around local noon till early afternoon, and gradual weakening in the late afternoon. Each day is different with respect to the details of the CBL evolution, depth, and decay. Within the CBL, $\overline{w'^2}$, $\bar{e}$, and $\overline{\varepsilon_{obs}}$ increase during the growth and peak phase. They weaken during the decay phase. $\overline{\tau_{w'}}$ also increases rapidly after sunrise and remains largest between 1000 and 1700 UTC, reflecting the period of strongest convection. $\overline{S_{w'}}$ is a measure of asymmetry in the vertical turbulent transport affected by TKE. $\overline{S_{w'}}$ is mostly positive during daytime, indicating stronger, narrower updrafts and weaker, broader

downdrafts, which is a typical characteristic of a buoyancy-driven CBL (e.g. Behrendt et al. 2015; Berg et al. 2017).

Within the daily cycles of each day and between the days there is substantial temporal and spatial variability of the turbulence variables, which is due to different meteorological conditions as well because of the stochastic behavior of turbulence and their sampling statistics. Therefore, it is interesting to study a larger data set of these variables over several days, as done in this study, to gain deeper insight into their statistics.

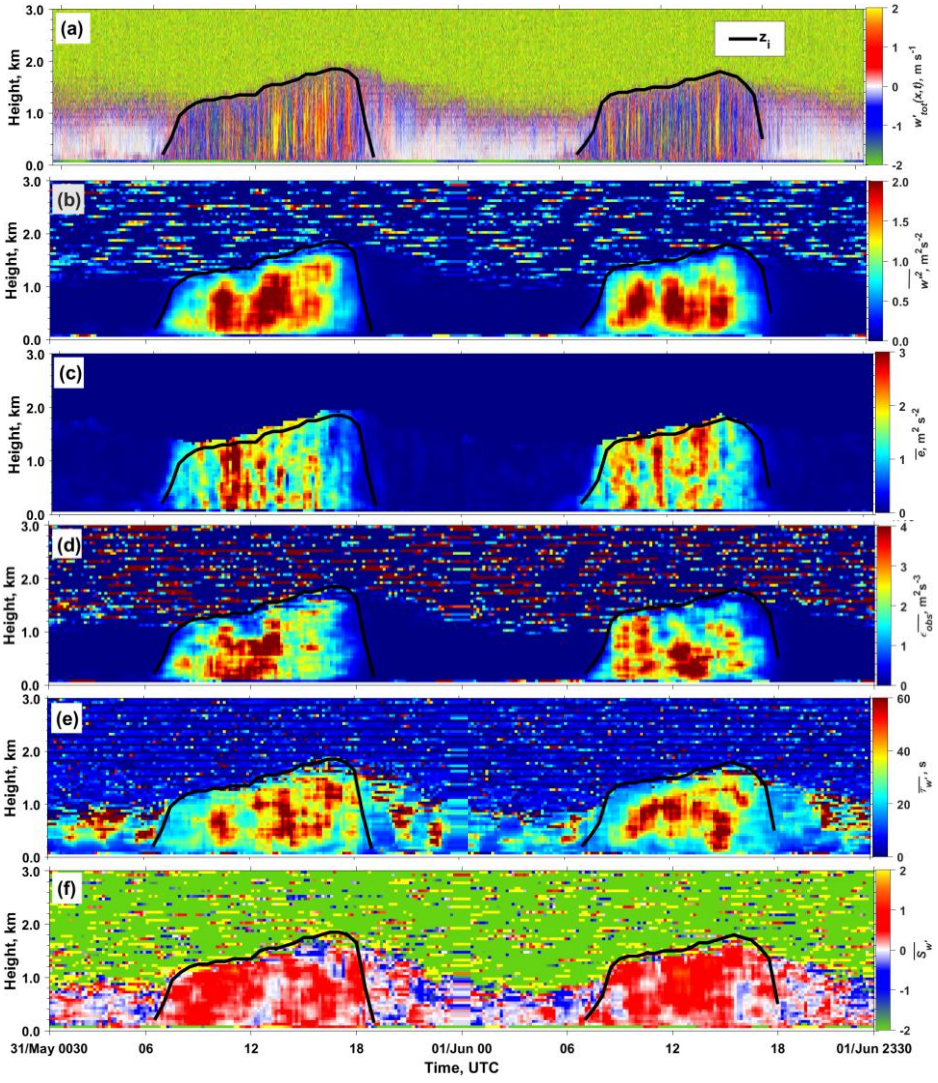


Fig. 5 The time height cross-section of (a) vertical wind velocity $w'_{tot}(z,t)$, (b) atmospheric vertical wind variance $\overline{w'^2}$, (c) $\bar{\varepsilon}$, (d) TKE dissipation $\bar{\varepsilon}$, (e) integral time scale $\overline{\tau_{w'}}$, and (f) vertical velocity skewness $\overline{S_w}$, shown for two days as an example: 31 May and 1 June 2021

Figure 6 shows profiles of the mean horizontal wind speed $\overline{V_h}$ and mean horizontal wind direction $\overline{\theta_h}$, obtained from six-beam DL time series at 21 m spatial and 90 s temporal

resolution. As it is typical, $\overline{V_h}$ remains nearly constant throughout daytime, and $\overline{\theta_h}$ exhibits only small fluctuations. We see a significant low-level jet peaking between 500 and 600 m during nighttime, which is dissolved during daytime by the buildup of the CBL. During daytime, the horizontal wind weakens and shows higher variability, which is due to turbulent eddies.

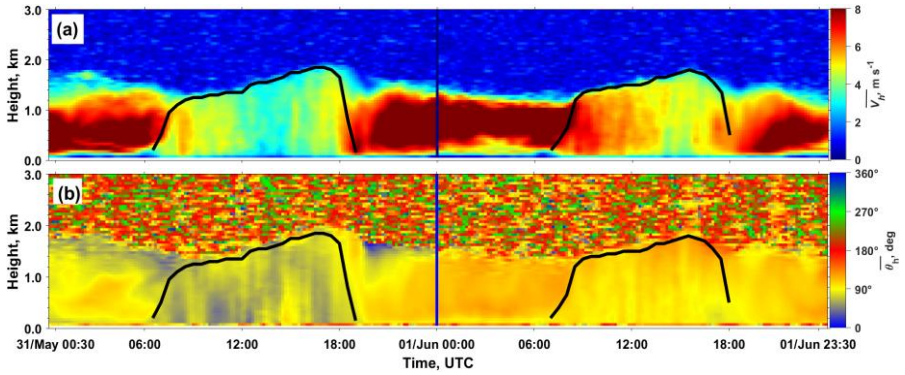


Fig. 6 Time height cross-section of (a) mean horizontal wind speed $\overline{V_h}$ and (b) mean horizontal wind direction $\overline{\theta_h}$ for the same period as in Fig. 5

4 Results with respect to Relationships between CBL Variables

4.1 CBL Dynamics: Vertical Wind Variance, TKE, TKE Dissipation, Integral Time Scales, and Horizontal Wind Speed Profiles

Figure 7 shows the distributions of $\overline{w'^2}$, $\overline{e}$, $\overline{\varepsilon_{obs}}$, $\overline{k_{w'}}$, $\overline{\tau_{w'}}$ and $\overline{V_h}$, against $z/\overline{z_i}$, at 1245 UTC for each selected day. The boxplots illustrate the daily variability in turbulent statistics during the peak convection. The median across all these days highlights the typical vertical turbulent structure.

The median profile of $\overline{w'^2}$ shows a peak value of 1.35 $m^2 s^{-2}$, typically around $0.40\overline{z_i}$, during the peak convective activity. At this height, the characteristic eddy size is 141 m. Likewise, the median profile of $\overline{\varepsilon_{obs}}$ peaks at 0.002 $m^2 s^{-3}$ appearing at $0.30\overline{z_i}$. This vertical structure closely resembles that of the median of $\overline{w'^2}$. In contrast, the median profile of $\overline{e}$ exhibits a peak value of 1.8 $m^2 s^{-2}$ in the upper CBL at 0.80 $\overline{z_i}$ with a turbulence length scale of 126 m, suggesting a more vertically extended turbulent structure due to wind shear. $\overline{\tau_{w'}}$ gradually increases from the surface, shows a peak value of 53.2 s at $0.63\overline{z_i}$, and

subsequently decreases toward the CBL top. $\overline{V_h}$ remains nearly constant at around 3 m s^{-1}, upto 0.80$\overline{z_i}$.

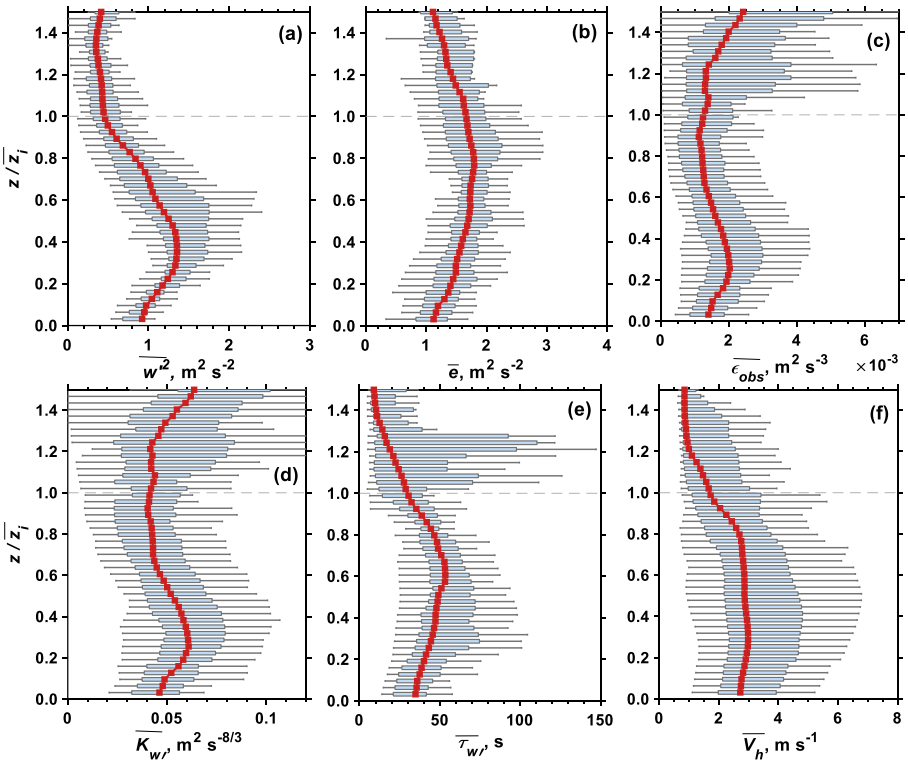


Fig. 7 Daily 30-min averaged profiles at 1245 UTC for all selected days from May to July 2021 and 2022: (a) $\overline{w'^2}$, (b) $\overline{e}$, (c) $\overline{\varepsilon_{obs}}$, (d) $\overline{k_{w'}}$, (e) $\overline{\tau_{w'}}$, and (f) $\overline{V_h}$. The median value at each height is marked with a red square. Light grey boxes indicate the 25th - 75th percentiles, and grey lines show the minimum and maximum values. Before averaging, each profile height is normalized by the corresponding CBL height $\overline{z_i}$

4.2 Mean Diurnal Evolution of Turbulence Structure in the CBL

Figure 8 shows the 30-min mean profiles of $\langle\overline{w'^2}\rangle$,$\langle\overline{e}\rangle$, $\langle\overline{\varepsilon_{obs}}\rangle$ from all selected days between 0900 to 1600 UTC, capturing the typical daytime evolution of turbulence within the CBL.

During the early growth of the CBL between 0900 and 1130 UTC, $\langle\overline{w'^2}\rangle$ expand vertically and gradually increase in magnitude as the surface heating intensifies. Over this period, the peak $\langle\overline{w'^2}\rangle$ values increased steadily from 0.93 m^2 s^{-2} to 1.5 m^2 s^{-2}, with peak values located near 0.37$\overline{z_i}$. Following this trend, the maximum $\langle\overline{w'^2}\rangle$ reaches 1.56 m^2 s^{-2} at 0.37$\overline{z_i}$ at 1200 UTC, just after local noon. In the afternoon between 1300 to 1600 UTC, $\langle\overline{w'^2}\rangle$ peaks gradually decrease from 1.34 to 0.67 m^2 s^{-2}, approximately at 0.37$\overline{z_i}$, reflecting the decline

in surface heating and weakening of turbulence mixing. The median profiles of $\langle\overline{e}\rangle$ follow a similar diurnal pattern, but with a distinct vertical evolution. At 0900 UTC, $\langle\overline{e}\rangle$ peaks at 1.15 $m^2\ s^{-2}$ near $0.47\overline{z_i}$, reflecting the early development of the CBL. By 1130 UTC, the peak value increases to 1.94 $m^2\ s^{-2,}$ and the peak location shifts upward to approximately $0.72\overline{z_i}$. The maximum $\langle\overline{e}\rangle$ of 2.0 $m^2\ s^{-2}$ is reached at 1200 UTC, at $0.67\overline{z_i}$. In the afternoon, from 1300 to 1600 UTC, $\langle\overline{e}\rangle$ gradually decreases from 1.66 to 0.93 $m^2\ s^{-2}$, with peak values occurring between $0.70\text{-}0.90\overline{z_i}$. The median $\langle\overline{\varepsilon_{obs}}\rangle$ profiles also follow a similar diurnal pattern. During the early-stage development of the CBL, at 0900 UTC, $\langle\overline{\varepsilon_{obs}}\rangle$ peaks at 1×10^{-3} $m^2\ s^{-3}$ near $0.32\overline{z_i}$. As surface heating increases, the peak value increases steadily to 2×10^{-3} $m^2\ s^{-3}$ near $0.27\overline{z_i}$ at local noon. Between 1300 to 1500 UTC, $\langle\overline{\varepsilon_{obs}}\rangle$ peaks gradually decline from 2×10^{-3} to 1×10^{-3} $m^2\ s^{-3}$ around $0.25\overline{z_i}$. Generally, it can be stated that the location of the maximum of these turbulent variables remains rather constant with respect to $z/\overline{z_i}$. These are interesting results for comparisons with models.

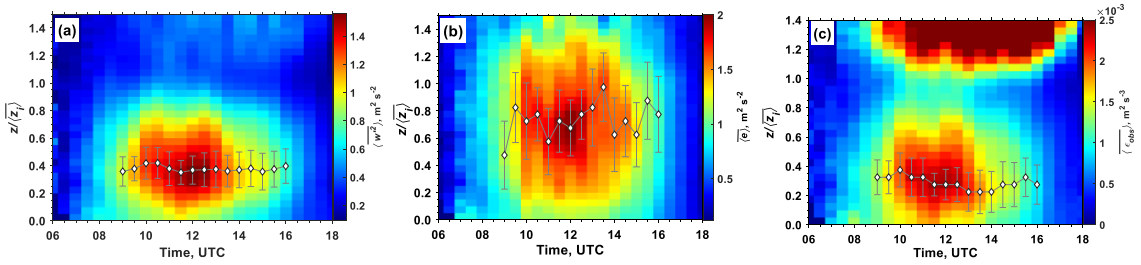


Fig. 8 Time-height plots showing the 30-min mean profiles over all selected days (a) $\langle\overline{w'^2}\rangle$, (b) $\langle\overline{e}\rangle$, and (c) $\langle\overline{\varepsilon_{obs}}\rangle$, from May-July for 2021 and 2022, between 0900 and 1600 UTC. The maximum of each of the turbulent quantities are highlighted with white-filled diamond markers. Error bars denote ± 1 standard deviation of the daily peak height ($z/\overline{z_i}$) distribution

4.3 Relationship between Vertical Wind Variance, TKE, and TKE dissipation

Between May and July, sunrise generally occurs between 0320 and 0400 UTC, while sunset occurs between 1840 and 1930 UTC. The most robust turbulent structure is observed from 0900 to 1600 UTC; we extend the analysis to 0600-1800 UTC to capture the full diurnal evolution of the CBL, including its early growth, peak development, and late-afternoon decay. This period captures the full daytime evolution, including transitions between CBL regimes, providing a more robust analysis of the relationships among the turbulence variables.

4.3.1 Relationship between Vertical Wind Variance, and TKE

Figure 9 shows the daily 30-min mean relationship between $\overline{w'^2}$ and $\overline{e}$ for all selected days during daytime hours (0600 to 1800 UTC). Normally, as $\overline{w'^2}$ increases, $\overline{e}$ also increases, which is expected due to their direct relationship.

Figure 9a shows that the RPD is highest (0.6-1.0) at low to moderate values of $\overline{w'^2}$ and $\overline{e}$. The largest RPD of $\overline{w'^2}$ and $\bar{e}$ occur near 0.3 $m^2 s^{-2}$ and 0.5 $m^2 s^{-2}$, respectively. Figure 10b shows that the coupling between $\overline{w'^2}$ and $\overline{e}$ is stronger in the lower CBL ($0.5 \leq z/\overline{z_i}$), with a correlation coefficient of r=0.69, while the upper CBL exhibits larger scatter and weaker correlation (r=0.53). This suggests a greater influence of wind shear on TKE in the upper CBL than in the lower CBL.

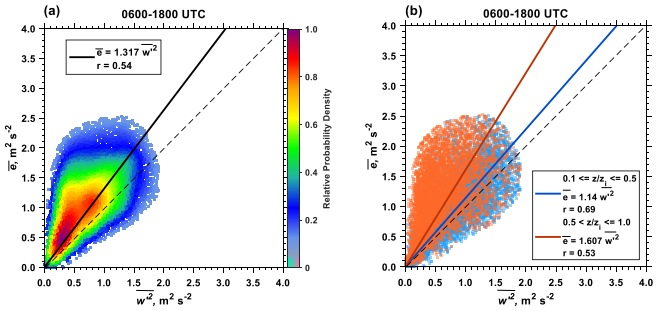


Fig. 9 Relationship between 30-min-averaged $\overline{w'^2}$ and $\overline{e}$, for all selected daytime period (0600-1800 UTC) within the entire CBL ($0.1 \leq z/\overline{z_i} \leq 1.0$). (a) Relative probability density distribution between 0.1 and 1.0. (b) Separation of the relationship into the lower CBL ($0.1 \leq z/\overline{z_i} \leq 0.5$) and upper CBL ($0.6 \leq z/\overline{z_i} \leq 1.0$) CBL

4.3.2 Relationship of TKE and Vertical Wind Variance with TKE Dissipation

In most turbulence-closure schemes, TKE dissipation is parameterized as a function of TKE, implicitly assuming that the horizontal and vertical components contribute uniformly to dissipation. Therefore, it is important to evaluate the relationship between TKE and TKE dissipation in the entire CBL.

Figures 10a and 10d show the daily 30-min mean relationships of $\overline{e}$ and $\overline{w'^2}$ with $\overline{\varepsilon_{obs}}$ for all selected days during daytime hours (0600 to 1800 UTC). The relationship between $\overline{e}$ and $\overline{\varepsilon_{obs}}$ is positive and non-linear, described by a power-law fit with r=0.52. Similar to the relationship between $\overline{w'^2}$ and $\bar{e}$, the relationship between $\overline{\varepsilon_{obs}}$ and $\overline{e}$ also exhibits a strong diurnal pattern. The lower values of these two quantities occur mostly in the early morning and late afternoon, while the largest values are observed from late morning to early afternoon. The RPD is highest (0.6-1.0) at low to moderate values of $\overline{e}$ (0.15-1.3 m^2

s^{-2}) and $\overline{\varepsilon_{obs}}$ ((1.7-8.0) × 10^{-4} m^2 s^{-3}). The largest RPD of $\overline{e}$ and $\overline{\varepsilon_{obs}}$ occur near 0.46 m^2 s^{-2} and 2.0 × 10^{-4} m^2 s^{-3}, respectively. As shown in Fig. 10b, $\overline{e}$ and $\overline{\varepsilon_{obs}}$ are strongly correlated in the lower CBL ($0.5 \leq z/\bar{z}_i$), with r=0.68, but the relationship weakens in the upper CBL (r=51).

Since the relationship between $\overline{e}$ and $\overline{\varepsilon_{obs}}$ is stronger in the lower CBL, a similarly strong correlation is observed between $\overline{w'^2}$ and $\overline{e}$, suggesting a close link between vertical wind variance and TKE dissipation in the CBL.

Figures 10c and 10d show the relationship between $\overline{w'^2}$ and $\overline{\varepsilon_{obs}}$ throughout the normalized height range $0.1 \leq z/\bar{z}_i \leq 1.0$ during daytime hours (0600-1800 UTC) for all selected days. Normally, higher $\overline{w'^2}$ values are associated with increased dissipation during the peak turbulence period around noon and in the afternoon, whereas lower values correspond to weaker turbulence in the early morning and the late afternoon. The highest RPD values are found at low to moderate values of $\overline{w'^2}$ and $\overline{\varepsilon_{obs}}$, within ranges of 0.1 - 0.6 m^2 s^{-2}, and 6.3×10^{-5} - 6.0×10^{-4} m^2 s^{-3}, respectively. Within these ranges, the observations follow the fitted power-law relationship more closely. For the entire CBL, $\overline{w'^2}$ also shows a much stronger nonlinear relationship with $\overline{\varepsilon_{obs}}$, with the power-law fit giving r=0.83. The higher correlation indicates that $\overline{w'^2}$ is more closely related to the observed TKE dissipation than TKE under the convective conditions considered here.

Figure 10d shows that the 3/2 power-law relationship between $\overline{w'^2}$ and $\overline{\varepsilon_{obs}}$ remains strong in both the lower and upper CBL, with correlation coefficients of 0.81 and 0.83, respectively. Although the individual data points show some dispersion, the overall trend follows the power-law scaling derived by Wulfmeyer et al. (2024) using autocovariance analysis. This agreement supports the physical relevance of $\overline{w'^2}$ as a proxy for turbulence dissipation in the daytime CBL.

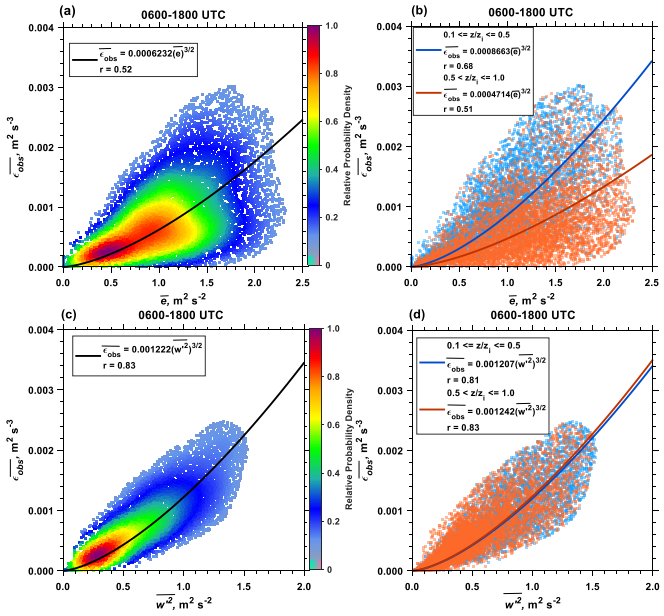


Fig. 10 Same as Fig.9, but showing the 3/2 power-law relationships of $\overline{e}$ and $\overline{w'^2}$ with $\overline{\varepsilon_{obs}}$

4.3.3 Influence of Convective Boundary Layer Depth and Surface Fluxes on the Relationship between $\overline{w'^2}$ and $\overline{\varepsilon_{obs}}$

To analyze the influence of surface forcing and boundary layer depth on the $\overline{w'^2}$ - $\overline{\varepsilon_{obs}}$ relationship, established in Sect. 4.3.2, the analysis was restricted to data within the CBL using a RPD threshold of $0.1 \leq RPD \leq 1.0$. An eddy-covariance (EC) station located about 600 m from the remote sensing site measures standard meteorological and high-resolution turbulent data at 2 m above canopy height at the LAFO site. The high-resolution flux measurements are collected using a Campbell Scientific CSAT3 sonic anemometer and a Licor 7500 gas analyzer. From these 10 Hz data, 30-min surface fluxes, such as sensible heat flux $\overline{H}$, and latent heat flux $\overline{LE}$ are estimated using the TK3 software package developed by Mauder and Foken, (2015). For data quality control, we have used the flag system of Mauder et al. (2013) for $\overline{H}$, and $\overline{LE}$, we exclude any data that falls outside of -100 W m^{-2} to 800 W m^{-2}.

$\overline{\varepsilon_{obs}}$ was scaled by the concurrent $\overline{H}$, $\overline{Q_n}$, $\overline{LE}$, and $\overline{z_i}$. The normalization relationships $\overline{\varepsilon_{obs}}/\overline{H}$, $\overline{\varepsilon_{obs}}/\overline{Q_n}$, $\overline{\varepsilon_{obs}}/\overline{LE}$, and $\overline{\varepsilon_{obs}}/\overline{z_i}$ were examined to assess whether variations in surface forcing and boundary layer depth account for part of the scatter in the $\overline{w'^2}$ - $\overline{\varepsilon_{obs}}$ relationship.

As shown in Fig. 11, normalizing $\overline{\varepsilon_{obs}}$ individually by $\overline{H}$, $\overline{Q_n}$, $\overline{LE}$ and $\overline{z_i}$ weakens its relationship with $\overline{w'^2}$. Compared with r=0.83 for the unscaled $\overline{w'^2}$ - $\overline{\varepsilon_{obs}}$ relationship, the corresponding correlation coefficient decreases to 0.05, 0.50, 0.56, and 0.58, respectively. These results show that, under condition examined, surface forcing and boundary layer depth do not improve the relationship when included as additional scaling variables.

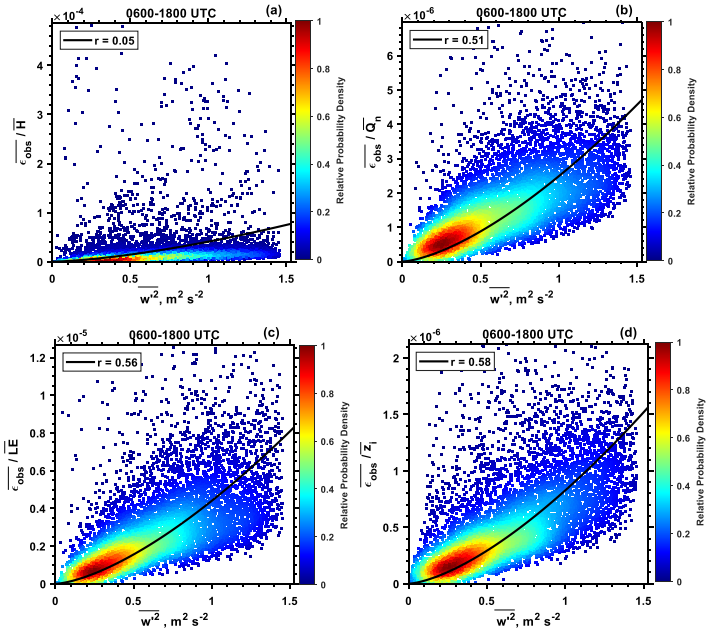


Fig. 11 Daily 30-min averaged scaled dissipations (a) $\overline{\varepsilon_{obs}}/\overline{H}$, (b) $\overline{\varepsilon_{obs}}/\overline{Q_n}$, (c) $\overline{\varepsilon_{obs}}/\overline{LE}$, and (d) $\overline{\varepsilon_{obs}}/\overline{z_i}$ plotted against $\overline{w'^2}$ for all selected days between 0600 and 1800 UTC. The fitted power-law curves and corresponding correlation coefficients are also shown

4.3.4 Comparison of TKE Dissipation Parametrizations using TKE and Vertical Wind Variance

As we have observed a moderate relationship between $\overline{e}$ and $\overline{\varepsilon_{obs}}$, and a strong relationship between $\overline{w'^2}$ and $\overline{\varepsilon_{obs}}$, we evaluate two dissipation parameterizations: a TKE-based formulation $\overline{\varepsilon_e} = \frac{(\overline{e})^{3/2}}{(C_e \overline{L_T})}$, and a $\overline{w'^2}$-based formulation, $\overline{\varepsilon_w} = \frac{(\overline{w'^2})^{3/2}}{(C_w \overline{L_T})}$.

The coefficients C_e=9.05 and C_w=4.4 were determined from the observations, and the parameterized dissipation rates were compared with $\overline{\varepsilon_{obs}}$. We analyze how well each formulation reproduces $\overline{\varepsilon_{obs}}$ within the CBL.

Figure 12 shows the diurnal evolution of the normalized Mellor-Yamada dissipation length scale $\overline{L_T}$ between 0600 to 1800 UTC within the CBL. $\overline{L_T}$ shows a pronounced diurnal cycle,

increasing in the morning, reaching a maximum value of 209 m at 1515 UTC, and then gradually decreasing towards 1800 UTC.

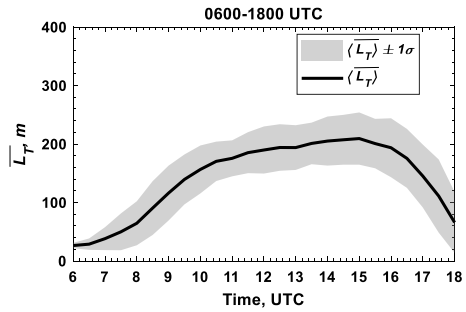


Fig. 12 Daily 30-min averaged diurnal evolution of $\overline{L_T}$ for all selected days between 0600 and 1800 UTC. The grey area represents ± standard deviation

Figure 13 compares the TKE and $\overline{w'^2}$ based dissipation parameterizations with $\overline{\varepsilon_{obs}}$ within the CBL. In Figure 13a, the relationship between $\overline{\varepsilon_e}$ and $\overline{\varepsilon_{obs}}$ is positive and linear, but weaker, with a correlation coefficient of 0.46. Observations during early morning and late afternoon are less scattered, while greater variability is observed around noon through the afternoon. The maximum RPD is found at 2.0×10^{-4} m^2 s^{-3}. This relationship is separated into the lower CBL and upper CBL, with correlation coefficients of 0.61 and 0.48, respectively. This shows that the TKE-based parameterization works relatively better in the lower CBL, where turbulence is locally produced and surface-driven, and more directly linked to the turbulent energy cascade. In the upper part of the CBL, entrainment, the capping-inversion effect, nonlocal transport, larger wind shear, and anisotropic organized TKE structure. However, overall, it does not robustly represent the observed TKE dissipation across the entire CBL. Beyond the standard TKE-based parameterization, we also evaluate $\overline{\varepsilon_w}$.

Figure 13c shows that $\overline{\varepsilon_w}$ is strongly positively correlated with $\overline{\varepsilon_{obs}}$ and performs well across the entire CBL, with reduced scatter and a correlation coefficient of r=0.79. The highest RPD values occur at low to moderate values of both $\overline{\varepsilon_w}$ and $\overline{\varepsilon_{obs}}$, with RPD decreasing as both quantities increase. Partitioning the entire CBL into lower and upper CBL shows the same correlation in both regions, with r=0.77. This supports the physical consistency of using $\overline{w'^2}$ as an alternative basis for TKE dissipation parameterization, rather than TKE itself. However, there was a slight reduction in correlation from 0.83 to 0.79 after including $\overline{L_T}$.

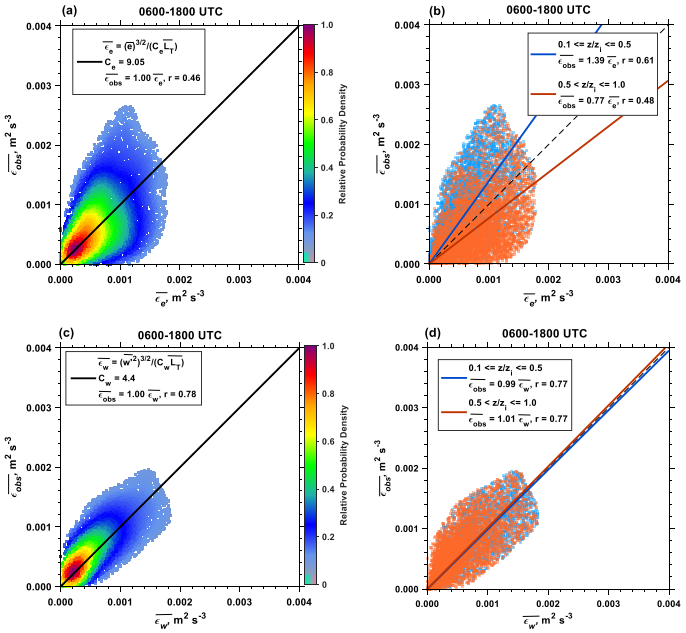


Fig. 13 Comparison of 30-min-averaged parametrized and observed TKE dissipation rates for all selected days during daytime (0600-1800 UTC) within the entire CBL ($0.1 \leq z/\overline{z_i} \leq 1.0$). (a)TKE-based parametrization, $\overline{\varepsilon_e}$ versus $\overline{\varepsilon_{obs}}$, with relative probability density and linear fit, (b) corresponding relationship for the lower and upper CBL. (c) Vertical wind variance-based parametrization, $\overline{\varepsilon_w}$ versus $\overline{\varepsilon_{obs}}$, with relative probability density and linear fit. (d) Corresponding relationship for the lower and upper CBL, each with a separate linear fit

4.3.5 Prediction of TKE dissipation using Random Forest and Multilayer Perceptron Models

We evaluate the ability of ML models to predict TKE dissipation in the CBL and identify the most influential physical variables. This enables us to search for more general relationships between $\overline{\varepsilon_{obs}}$ and driving variables. We used two ML models: a Random Forest (RF), an ensemble tree-based regression model, and a multilayer perceptron (MLP), a feedforward neural network. For the RF model, the main hyperparameters were the ensemble size (350), the minimum terminal node size (5), and the number of predictors examined at each split. The MLP model used two hidden layers with 12 and 8 neurons and trained using the scaled conjugate gradient algorithm for 600 epochs. To avoid overfitting, 20% of complete days (5 days) were randomly selected for validation, while the remaining 80% (20 days) were used for model training. As input, we used daytime data between 06:00 and 18:00 UTC, with 30-min mean quantities derived from DLs and an EC station: $\overline{w'^2}$, $\overline{e}$, $\overline{z_i}$, $\overline{H}$, and $\overline{Q_n}$. All variables were log-transformed before training. Both models were

trained and evaluated using the same data split, with 8332 samples used for training and 2269 samples used for validation.

Figure 14a shows the scatter plot between $\overline{\varepsilon_{obs}}$ and $\overline{\varepsilon_{pred}}$, indicating good agreement for both RF and MLP models. Most of the data points are closely aligned with the 1:1 line, with correlation coefficients of 0.83 for the RF and 0.84 for the MLP. However, the larger deviations from the 1:1 line occur for a few higher values of observed TKE dissipation, where both models tend to underestimate $\overline{\varepsilon_{obs}}$. Figure 14b confirms that $\overline{w'^2}$ is the most important and dominant predictor of $\overline{\varepsilon_{pred}}$ in both models, contributing about 47% of the total importance in RF and nearly 93% in the MLP model. In the RF models, the remaining feature importance is distributed among $\overline{z_i}$ (17%), $\overline{e}$ (12.5%), $\overline{H}$ (12%), and $\overline{Q_n}$ (11%), each of these contributes less significantly.

In the MLP model, $\overline{e}$ is the second most important predictor, contributing just 5%. The difference in feature importance between the RF and MLP models reflects their way of capturing nonlinear patterns. Although the MYNN scheme traditionally uses e as the primary predictor for TKE dissipation, our results show that $\overline{w'^2}$ is a stronger and more physically meaningful predictor in the CBL.

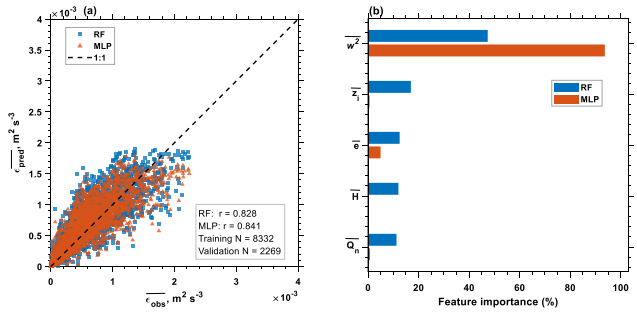


Fig. 14 (a) Scatter plot of the relationship between $\overline{\varepsilon_{pred}}$ and $\overline{\varepsilon_{obs}}$ shows the results from both the RF and MLP, along with the 1:1 reference line. (b) Bar plot of feature importance from RF and MLP models, showing the relative contribution of $\overline{w'^2}$, $\overline{e}$, $\overline{z_i}$, $\overline{H}$, $\overline{Q_n}$ to TKE dissipation prediction

5. Discussion

In this study, we observe that the 30-min median profiles of $\overline{w'^2}$, $\overline{e}$, and $\overline{\varepsilon_{obs}}$ show the expected three-phase diurnal evolution of convective turbulence (growth, peak, and decay) between 0900 and 1600 UTC for all selected days. During this period, the mean location of the 30-min maxima in $\overline{w'^2}$ exhibits a peak at $0.34\overline{z_i}$, indicating that the strongest

turbulent motions occur in the lower to the middle part of the CBL. This peak height is consistent with the widely reported range of 0.3-0.4 $\overline{z_i}$ observed in previous studies (Lenschow et al. 2000; Lenschow et al. 2012; Dewani et al. 2023; Wulfmeyer et al. 2024). However, Berg et al. (2017) reported a slightly lower peak at 0.25$\overline{z_i}$. The small discrepancy in the peak height across these studies may be attributed to differences in meteorological conditions, stability conditions, lidar sampling strategies, and the method used for determining $\overline{z_i}$. Similarly, the mean location of 30-min maxima in $\overline{\varepsilon_{obs}}$ occurs at 0.29$\overline{z_i}$, slightly below the peak reported by Wulfmeyer et al. (2024). The proximity of these maxima indicates a strong association between vertical turbulent motions and the dissipation of turbulent kinetic energy. In contrast, total TKE reached its mean maximum at 0.73$\overline{z_i}$, significantly higher in the CBL than the peak in vertical wind variance and TKE dissipation. Previous LES studies showed that while normalized $\overline{w'^2}$ exhibits a relatively universal vertical profile, horizontal wind variance varies more strongly with stability and height, significantly influencing the vertical structure of total TKE (Zhou et al. 2019). Zhang et al. (2026) showed that strong wind shear increases TKE near the CBL top within the entrainment zone. BLLAST support this finding as well, showing distinct vertical behaviors of the velocity components, particularly in the upper CBL during the afternoon transition (Darbieu et al. 2015). The peak in total TKE occurs near the CBL top, driven by enhanced entrainment and wind shear that amplifies horizontal wind variance, whereas $\overline{w'^2}$ and $\overline{\varepsilon_{obs}}$ peak in the lower to middle CBL, where buoyancy-driven turbulence dominates. This vertical separation reflects the contrasting roles of convective updrafts (lower CBL) and shear-induced motions (upper CBL). These patterns are consistent with prior observational and modeling studies (Zhou et al. 2019, 2020; Fodor and Mellado 2020; Lv et al. 2023; Zhang et al. 2026).

The different locations of these maxima show that the relationship between TKE, $\overline{w'^2}$, and TKE dissipation are not uniform throughout the CBL. In the lower half of the CBL ($0.1 \leq z/\overline{z_i} \leq 0.5$), strong relationships are observed between $\overline{e}$ and $\overline{w'^2}$, as well as between $\overline{e}$ and $\overline{\varepsilon_{obs}}$, indicating a dominant role of buoyancy-driven vertical motions in the turbulence cascade in the inertial subrange. These relationships weaken in the upper half of the CBL ($0.6 \leq z/\overline{z_i} \leq 1.0$), where turbulence is less influenced by the surface buoyancy and more

affected by wind shear within the entrainment zone, entrainment and large-scale dynamics (Zhang et al. 2026). The difference observed in vertical distributions of TKE, $\overline{w'^2}$,and $\overline{\varepsilon_{obs}}$, together with their changing relationships in the lower and upper CBL, provides a physical basis for further evaluating TKE dissipation parametrization. The comparison between $\overline{\varepsilon_{obs}}$ and TKE dissipation derived from the MYNN *e*-dissipation $\overline{\varepsilon_e}$ formulation highlights the limitations of using *e* to parametrize TKE dissipation. The correlation between $\overline{\varepsilon_{obs}}$ and $\overline{\varepsilon_e}$ is relatively weak, indicating that this turbulence scheme does not fully capture the observed variability of TKE dissipation in clear-sky convective conditions, likely due to contamination from organized convection. This finding is consistent with the interpretation proposed by Zhou et al. (2019, 2020) and subsequently supported by Lv et al. (2023): conventional TKE-based dissipation scaling can be biased when total TKE includes energy associated with organized convective structures that does not participate in the inertial-range energy cascade. Motivated by these findings, replacing $\boldsymbol{e}$ with $\overline{w'^2}$ in the same MYNN TKE dissipation formulation, while keeping the same turbulence length scales derived from *e*, significantly improves the correlation with $\overline{\varepsilon_{obs}}$. Therefore, we suggest adding another prognostic equation in turbulence parameterizations, namely the vertical wind budget equation. The analysis of the $\overline{\varepsilon_{obs}} - \overline{w'^2}$ relationship confirms the expected inertial-subrange scaling of the form $\varepsilon \propto (\overline{w'^2})^{3/2}$, as proposed by Wulfmeyer et al. (2024). The observed power-law relationship between TKE dissipation and $\overline{w'^2}$ is robust across the analysed clear-sky convective days. Furthermore, we tested the normalization of $\overline{\varepsilon_{obs}}$ with CBL depth, sensible heat flux, and net radiation, but the correlation did not improve. Both the MLP and RF consistently identify $\overline{w'^2}$ as the dominant predictor of the TKE dissipation, while bulk *e*, CBL depth, and surface fluxes play only a minor role. However, both models tend to underestimate the largest dissipation values, which are likely to reflect the limited number of extreme cases and higher uncertainty at very high $\overline{\varepsilon_{obs}}$ values.

We conclude that the process-based analysis and the ML results indicate a consistent picture: in clear-sky daytime CBL, vertical wind variance provides a more direct and physically consistent basis for parameterizing TKE dissipation rather than $\boldsymbol{e}$. This suggests a revision of MYNN-type schemes towards a $\overline{w'^2}$-based dissipation closure, using the formulation form

$$\overline{\varepsilon_w} \sim \frac{\left(\overline{w'^2}\right)^{3/2}}{(C_w\,\overline{L_T})}.$$

However, incorporating $\overline{L_T}$ slightly weakened the relationship between the observed TKE dissipation and vertical wind variance. This suggests that the bulk TKE-derived length scale does not fully capture the local length scale variability relevant to dissipation within the CBL, consistent with the limitations of scaling-based dissipation length formulation discussed by Zhou et al. (2020).

It should be noted that these conclusions are based on a specific site and on a subset of well-developed convective cases. This strongly motivates for testing $\overline{w'^2}$-based dissipation formulations more broadly. In the future, one should also explore height and stability-dependent dissipation scales that account for varying influences of buoyancy, wind shear, and entrainment within the CBL. We foresee, that a combination of long-term, high-resolution Doppler lidar observations and machine learning will offer a framework for such tests and for further refinement of turbulence closure approaches in numerical weather prediction and LES models.

6. Summary and Outlook

This study highlights the benefits of combining vertical-pointing and six-beam scanning Doppler lidars for the detailed analysis of the CBL characterization. Following Wulfmeyer et al. (2016, 2024), the transverse temporal ACF of vertical wind fluctuations from a vertical-pointing Doppler lidar is used to derive $\overline{w'^2}$, ε, $k_{w'}$, $\tau_{w'}$ and R_w. The profiles of V_h and e are derived from the six-beam scanning Doppler lidar data using the method of Bonin et al. (2017). The analysis is restricted to clear-sky, rain-free, and nearly cloud-free days from May-July 2021 and 2022, between 0600 and 1800 UTC. These multi-day datasets enable a detailed examination of turbulence in the CBL and provide a robust basis for evaluating TKE dissipation parameterization in boundary layer schemes.

Between 0900 and 1600 UTC, the 30-min average median profiles of $\overline{w'^2}$, $\overline{e}$, and $\overline{\varepsilon_{obs}}$ show a well-defined diurnal evolution of turbulence in the CBL. During this period, the mean peak values of $\langle\overline{w'^2}\rangle$, $\langle\overline{e}\rangle$, and $\langle\overline{\varepsilon_{obs}}\rangle$, occur at $0.34\overline{z_i}$, $0.73\overline{z_i}$, and $0.29\overline{z_i}$, respectively. The vertical structure of these turbulent quantities is consistent with previous observational

and modelling studies. In the lower CBL ($0.1 \leq z/\overline{z_i} \leq 0.5$), $\overline{e}$ shows strong relationships with both $\overline{w'^2}$ and $\overline{\varepsilon_{obs}}$, with a correlation coefficient of approximately 0.70. These relationships weaken in the upper CBL ($0.6 \leq z/\overline{z_i} \leq 1.0$), where the correlation decreases to about 0.52. A power-law scaling relationship of the form $\overline{\varepsilon_{obs}} \propto (\overline{w'^2})^{3/2}$ achieves an even higher correlation of approximately 0.83 across the entire CBL. Our results indicate that replacing e with $\overline{w'^2}$ as the primary variable in TKE dissipation parametrization significantly improves agreement with observations, increasing the correlation from approximately 0.46 (using e-based dissipation parametrization) to about 0.80 (using $\overline{w'^2}$-based dissipation parametrization). Machine learning analyses using RF and MLP confirm $\overline{w'^2}$ as the primary predictor of TKE dissipation, while $\overline{e}$,, $\overline{z_i}$, $\overline{H}$, and $\overline{Q_n}$ play a secondary role. Taking together, these results support a revisit of MYNN-type dissipation parametrization by using $\overline{w'^2}$ based scaling ($\varepsilon_w \sim (\overline{w'^2})^{3/2} / C_w \overline{L_T}$) with turbulent dissipation length scale using e. However, further refinement of the dissipation length scale is needed to account for its height and stability dependence within the CBL.

Future work should test this revised formulation under a wider range of atmospheric conditions, including strong wind shear, entrainment processes, stability dependence, surface heterogeneity, cloud-topped boundary layer, and different seasons of the year. This also highlights the potential of combining long-term lidar observations with machine learning to refine turbulence closures in numerical weather prediction and LES models.

Acknowledgments

We gratefully acknowledge the Carl Zeiss Foundation for funding the setup phase of LAFO through its program to enhance research infrastructure at the University of Hohenheim. We also like to thank Florian Späth for his support of the measurements. This work was supported by the DFG via grant WU 356/28-1, within the scope of the Research Unit 5639 "Land-Atmosphere Feedback Initiative".

Code/Data availability

Code/Data are available upon request from the corresponding author.

Author contributions

The turbulent measurement strategy has been designed and supervised by Volker Wulfmeyer and Andreas Behrendt. The codes in IDL and Matlab for the data analysis were written by Syed Saqlain Abbas and Volker Wulfmeyer. The data analysis was mainly performed by Syed Saqlain Abbas. The eddy-covariance data were processed by Verena Rajtschan. All authors contributed to the discussion and writing of this paper.

Competing interests

The contact author has declared that none of the authors has any competing interests.

References

Banta RM, Pichugina YL, Kelley ND, Hardesty RM, Brewer WA (2013) Wind energy meteorology: insight into wind properties in the turbine-rotor layer of the atmosphere from high-resolution Doppler lidar. Bull Am Meteorol Soc 94:883–902. https://doi.org/10.1175/BAMS-D-11-00057.1

Behrendt A, Wulfmeyer V, Hammann E, Muppa SK, Pal S (2015) Profiles of second- to fourth-order moments of turbulent temperature fluctuations in the convective boundary layer: first measurements with rotational Raman lidar. Atmos Chem Phys 15:5485–5500. https://doi.org/10.5194/acp-15-5485-2015

Berg LK, Zhong S (2005) Sensitivity of MM5-simulated boundary layer characteristics to turbulence parameterizations. J Appl Meteorol 44:1467–1483. https://doi.org/10.1175/JAM2292.1

Berg LK, Newsom RK, Turner DD (2017) Year-long vertical velocity statistics derived from Doppler lidar data for the continental convective boundary layer. J Appl Meteorol Climatol 56:2441–2454. https://doi.org/10.1175/JAMC-D-16-0359.1

Bodini N, Lundquist JK, Optis M (2020) Can machine learning improve the model representation of turbulent kinetic energy dissipation rate in the boundary layer for complex terrain? Geosci Model Dev 13:4271–4285. https://doi.org/10.5194/gmd-13-4271-2020

Bodini, N., Lundquist, J. K., & Newsom, R. K. (2018). Estimation of turbulence dissipation rate and its variability from sonic anemometer and wind Doppler lidar during the XPIA field campaign. Atmospheric Measurement Techniques, 11, 4291–4308. https://doi.org/10.5194/amt-11-4291-2018

Bonin TA, Newman JF, Klein PM, Chilson PB, Wharton S (2016) Improvement of vertical velocity statistics measured by a Doppler lidar through comparison with sonic anemometer observations. Atmos Meas Tech 9:5833–5852. https://doi.org/10.5194/amt-9-5833-2016

Bonin TA, Choukulkar A, Brewer WA, Sandberg SP, Weickmann AM, Pichugina YL, Banta RM, Oncley SP, Wolfe DE (2017) Evaluation of turbulence measurement techniques from a single Doppler lidar. Atmos Meas Tech 10:3021–3039. https://doi.org/10.5194/amt-10-3021-2017

Bonin TA, Carroll BJ, Hardesty RM, Brewer WA, Hajny K, Salmon OE, Shepson PB (2018) Doppler lidar observations of the mixing height in Indianapolis using an automated composite fuzzy logic approach. J Atmos Ocean Technol 35:473–490. https://doi.org/10.1175/JTECH-D-17-0159.1

Bougeault P, Lacarrère P (1989) Parameterization of orography-induced turbulence in a mesobeta-scale model. Mon Weather Rev 117:1872–1890. https://doi.org/10.1175/1520-0493(1989)117%3C1872:POOITI%3E2.0.CO;2

Darbieu C, Lohou F, Lothon M, Vilà-Guerau de Arellano J, Couvreux F, Durand P, Pino D, Patton EG, Nilsson E, Blay-Carreras E, Gioli B (2015) Turbulence vertical structure of the boundary layer during the afternoon transition. Atmos Chem Phys 15:10071–10086. https://doi.org/10.5194/acp-15-10071-2015

Dewani N, Sakradzija M, Schlemmer L, Leinweber R, Schmidli J (2023) Dependency of vertical velocity variance on meteorological conditions in the convective boundary layer. Atmos Chem Phys 23:4045–4058. https://doi.org/10.5194/acp-23-4045-2023

Fodor K, Mellado JP (2020) New insights into wind shear effects on entrainment in convective boundary layers using conditional analysis. J Atmos Sci 77:3227–3248. https://doi.org/10.1175/JAS-D-19-0345.1

Holtslag AAM, Svensson G, Baas P, Basu S, Beare B, Beljaars ACM, Bosveld FC, Cuxart J, Lindvall J, Steeneveld GJ, Tjernström M, van de Wiel BJH (2013) Stable atmospheric

boundary layers and diurnal cycles: challenges for weather and climate models. Bull Am Meteorol Soc 94(11):1691–1706. https://doi.org/10.1175/BAMS-D-11-00187.1

Honnert R, Masson V, Couvreux F (2011) A diagnostic for evaluating the representation of turbulence in atmospheric models at the kilometric scale. J Atmos Sci 68:3112–3131. https://doi.org/10.1175/JAS-D-11-061.1

Hu X-M, Klein PM, Xue M (2013) Evaluation of the updated YSU planetary boundary layer scheme within WRF for wind resource and air quality assessments. J Geophys Res Atmos 118(18):10490–10505. https://doi.org/10.1002/jgrd.50823

Janjić ZI (1994) The step-mountain Eta coordinate model: further developments of the convection, viscous sublayer, and turbulence closure schemes. Mon Weather Rev 122:927–945. https://doi.org/10.1175/15200493(1994)122<0927:TSMECM>2.0.CO;2

Kaimal JC, Finnigan JJ (1994) Atmospheric boundary layer flows: their structure and measurement. Oxford University Press, New York, 304 pp.

Lampert A, Pätzold F, Jiménez MA, Lobitz L, Martin S, Lohmann G, Canut G, Legain D, Bange J, Martínez-Villagrasa D, Cuxart J (2016) A study of local turbulence and anisotropy during the afternoon and evening transition with an unmanned aerial system and mesoscale simulation. Atmos Chem Phys 16:8009–8021. https://doi.org/10.5194/acp-16-8009-2016

Lenschow DH, Stankov BB (1986) Length scales in the convective boundary layer. J Atmos Sci 43:1198–1209. https://doi.org/10.1175/1520-0469(1986)043%3C1198:LSITCB%3E2.0.CO;2

Lenschow DH, Wulfmeyer V, Senff C (2000) Measuring second- through fourth-order moments in noisy data. J Atmos Ocean Technol 17:1330–1347. https://doi.org/10.1175/1520-0426(2000)017%3C1330:MSTFOM%3E2.0.CO;2

Lenschow DH, Lothon M, Mayor SD, Sullivan PP, Canut G (2012) A comparison of higher-order vertical velocity moments in the convective boundary layer from lidar with in situ measurements and large-eddy simulation. Boundary-Layer Meteorol 143:107–123. https://doi.org/10.1007/s10546-011-9615-3

Li Z, Guo J, Ding A, Liao H, Liu J, Sun Y, Wang T, Xue H, Zhang H, Zhu B (2017) Aerosol and boundary-layer interactions and impact on air quality. Natl Sci Rev 4:810–833. https://doi.org/10.1093/nsr/nwx117

Lv Y, Muñoz-Esparza D, Chen X, Zhang C, Luo M, Wang R, Zhou B (2023) Stability dependence of the turbulent dissipation rate in the convective atmospheric boundary layer. Geophys Res Lett 50:e2023GL103326. https://doi.org/10.1029/2023GL103326

Mauder M, Cuntz M, Drüe C, Graf A, Rebmann C, Schmid HP, Schmidt M, Steinbrecher R (2013) A strategy for quality and uncertainty assessment of long-term eddy-covariance measurements. Agric For Meteorol 169:122–135. https://doi.org/10.1016/j.agrformet.2012.09.006

Mauder M, Foken T (2015) Eddy-covariance software TK3: documentation and instruction manual of the eddy-covariance software package TK3 (update). University of Bayreuth, Bayreuth, 67 pp. https://doi.org/10.5281/zenodo.20349

Mellor GL, Yamada T (1974) A hierarchy of turbulence closure models for planetary boundary layers. J Atmos Sci 31:1791–1806. https://doi.org/10.1175/1520-0469(1974)031%3C1791:AHOTCM%3E2.0.CO;2

Monin AS, Yaglom AM (1979) Statistical fluid mechanics: mechanics of turbulence, vols 1 and 2. MIT Press, Cambridge, MA

Nakanishi M, Niino H (2006) An improved Mellor–Yamada level-3 model: its numerical stability and application to a regional prediction of advection fog. Boundary-Layer Meteorol 119:397–407. https://doi.org/10.1007/s10546-005-9030-8

Nakanishi M, Niino H (2009) Development of an improved turbulence closure model for the atmospheric boundary layer. J Meteorol Soc Jpn Ser II 87:895–912. https://doi.org/10.2151/jmsj.87.895

National Center for Atmospheric Research (2026) WRF physics. WRF User's Guide. https://www2.mmm.ucar.edu/wrf/users/wrf_users_guide/build/html/physics.html. Accessed 14 Mar 2026

Newsom RK, Brewer WA, Wilczak JM, Wolfe DE, Oncley SP, Lundquist JK (2017) Validating precision estimates in horizontal wind measurements from a Doppler lidar. Atmos Meas Tech 10:1229–1240. https://doi.org/10.5194/amt-10-1229-2017

Newsom, R. K., Sivaraman, C., Shippert, T. R., Riihimäki, L., & Pacific Northwest National Laboratory (2019). Doppler lidar vertical velocity statistics value-added product. DOE/SC-ARM-TR-149. Pacific Northwest National Laboratory. https://www.arm.gov/publications/tech_reports/doe-sc-arm-tr-149.pdf

Nieuwstadt, F. T. M., and P. G. Duynkerke, 1996: Turbulence in the atmospheric boundary layer. Atmos. Res., 40, 111–142, https://doi.org/10.1016/0169-8095(95)00034-8

Nilsson, E., Lohou, F., Lothon, M., Pardyjak, E., Mahrt, L., & Darbieu, C. (2016). Turbulence kinetic energy budget during the afternoon transition – Part 1: Observed surface TKE budget and boundary layer description for 10 intensive observation period days. Atmospheric Chemistry and Physics, 16, 8849–8872. https://doi.org/10.5194/acp-16-8849-2016

O'Connor EJ, Illingworth AJ, Brooks IM, Westbrook CD, Hogan RJ, Davies F, Brooks BJ (2010) A method for estimating the turbulent kinetic energy dissipation rate from a vertically pointing Doppler lidar, and independent evaluation from balloon-borne in situ measurements. J Atmos Ocean Technol 27:1652–1664. https://doi.org/10.1175/2010JTECHA1455.1

Olson JB, Kenyon JS, Angevine WA, Brown JM, Pagowski M, Sušelj K (2019) A description of the MYNN-EDMF scheme and the coupling to other components in WRF-ARW. NOAA Technical Memorandum OAR GSD-61, NOAA Earth System Research Laboratory, Boulder. https://doi.org/10.25923/n9wm-be49

Renner M, Brenner C, Mallick K, Wizemann HD, Conte L, Trebs I, Wei J, Wulfmeyer V, Schulz K, Kleidon A (2019) Using phase lags to evaluate model biases in simulating the diurnal cycle of evapotranspiration: a case study in Luxembourg. Hydrol Earth Syst Sci 23:515–535. https://doi.org/10.5194/hess-23-515-2019

Sathe A, Mann J, Vasiljevic N, Lea G (2015) A six-beam method to measure turbulence statistics using ground-based wind lidars. Atmos Meas Tech 8:729–740. https://doi.org/10.5194/amt-8-729-2015

Smith EN, Carlin JT (2024) A multi-instrument fuzzy logic boundary-layer-top detection algorithm. Atmos Meas Tech 17:4087–4107. https://doi.org/10.5194/amt-17-4087-2024

Späth F, Rajtschan V, Weber TKD, Morandage S, Lange D, Abbas SS, Behrendt A, Ingwersen J, Streck T, Wulfmeyer V (2023) The land-atmosphere feedback observatory: a new observational approach for characterizing land-atmosphere feedback. Geosci Instrum Methods Data Syst 12:25–44. https://doi.org/10.5194/gi-12-25-2023

Steeneveld GJ, Mauritsen T, de Bruijn EIF, Vilà-Guerau de Arellano J, Svensson G, Holtslag AAM (2008) Evaluation of limited-area models for the representation of the diurnal cycle and contrasting nights in CASES-99. J Appl Meteorol Climatol 47:869–887. https://doi.org/10.1175/2007JAMC1702.1

Storm B, Dudhia J, Basu S, Swift A, Giammanco I (2009) Evaluation of the Weather Research and Forecasting Model on forecasting low-level jets: implications for wind energy. Wind Energy 12:81–90. https://doi.org/10.1002/we.288

Stull RB (1988) An introduction to boundary layer meteorology. Kluwer Academic Publishers, Dordrecht, 670 pp

Trier SB, Chen F, Manning KW (2004) A study of convection initiation in a mesoscale model using high-resolution land surface initial conditions. Mon Weather Rev 132:2954–2976. https://doi.org/10.1175/MWR2839.1

Tucker SC, Senff CJ, Weickmann AM, Brewer WA, Banta RM, Sandberg SP, Law DC, Hardesty RM (2009) Doppler lidar estimation of mixing height using turbulence, shear, and aerosol profiles. J Atmos Ocean Technol 26:673–688. https://doi.org/10.1175/2008JTECHA1157.1

Wilson JW, Roberts RD (2006) Summary of convective storm initiation and evolution during IHOP: observational and modeling perspective. Mon Weather Rev 134:23–47. https://doi.org/10.1175/MWR3069.1

Wu G, Zhang C, Zhao R, Qin P, Qin Y (2023) Asymmetries of the lag between air temperature and insolation in gauge observations and reanalyses over China. Atmos Res 288:106729. https://doi.org/10.1016/j.atmosres.2023.106729

Wulfmeyer V, Muppa SK, Behrendt A, Hammann E, Späth F, Sorbjan Z, Turner DD, Hardesty RM (2016) Determination of convective boundary layer entrainment fluxes, dissipation rates, and the molecular destruction of variances: theoretical description and a strategy for its confirmation with a novel lidar system synergy. J Atmos Sci 73:667–692. https://doi.org/10.1175/JAS-D-14-0392.1

Wulfmeyer V, Turner DD (2018) Land-Atmosphere Feedback Experiment field campaign report. DOE/SC-ARM-18-007, US Department of Energy, Office of Science, Washington, DC

Wulfmeyer, V., Späth, F., Behrendt, A., Jach, L., Warrach-Sagi, K., Ek, M., Turner, D. D., Senff, C., Ferguson, C. R., Santanello, J., Lee, T. R., Buban, M., & Verhoef, A. (2020). The GEWEX Land–Atmosphere Feedback Observatory (GLAFO). GEWEX Quarterly, 30(1), 6–11.

Wulfmeyer V, Senff C, Späth F, Behrendt A, Lange D, Banta RM, Brewer WA, Wieser A, Turner DD (2024) Profiling the molecular destruction rates of temperature and humidity as well as the turbulent kinetic energy dissipation in the convective boundary layer. Atmos Meas Tech 17:1175–1196. https://doi.org/10.5194/amt-17-1175-2024

Wyngaard, J. C. (2004). Toward numerical modeling in the “terra incognita.” Journal of the Atmospheric Sciences, 61(14), 1816–1826. https://doi.org/10.1175/1520-0469(2004)061<1816:TNMITT>2.0.CO;2

Yang B, Qian Y, Berg LK, Ma PL, Wharton S, Bulaevskaya V, Yan H, Hou Z, Shaw WJ (2017) Sensitivity of turbine-height wind speeds to parameters in planetary boundary-layer and surface-layer schemes in the Weather Research and Forecasting Model. Boundary-Layer Meteorol 162:117–142. https://doi.org/10.1007/s10546-016-0185-2

Zhang, H., Yin, J., He, Q., Wang, M., & Chen, Y. (2026). Entrainment in sheared dry convective boundary layers: The depth dependence. Journal of Geophysical Research: Atmospheres, 131, e2025JD045894. https://doi.org/10.1029/2025JD045894

Zhou B, Sun S, Sun J, Zhu K (2019) The universality of the normalized vertical velocity variance in contrast to the horizontal velocity variance in the convective boundary layer. J Atmos Sci 76:1437–1456. https://doi.org/10.1175/JAS-D-18-0325.1

Zhou B, Li Y, Zhu K (2020) Improved length scales for turbulence kinetic energy-based planetary boundary layer scheme for the convective atmospheric boundary layer. J Atmos Sci 77:2605–2626. https://doi.org/10.1175/JAS-D-19-0334.1